Biosensors and Bioelectronics 132 (2019) 55–61

Contents lists available at ScienceDirect

Biosensors and Bioelectronics

journal homepage: www.elsevier.com/locate/bios

A new photoelectrochemical immunosensor for ultrasensitive assay of prion protein based on hemin-induced photocurrent direction switching

Ruiying Yang[1], Kang Zou[1], Xiaohua Zhang, Cuicui Du, Jinhua Chen*

State Key Laboratory of Chemo/Biosensing and Chemometrics, College of Chemistry and Chemical Engineering, Hunan University, Changsha 410082, PR China

ARTICLE INFO

Keywords:
Hemin
CdS
Nitrogen-doped porous carbon
Prion protein
Photoelectrochemical immunosensor

ABSTRACT

As a significant biomarker of prion diseases, ultrasensitive assay of infectious isoform of prion (PrP^{Sc}) is highly desirable for early diagnostics of prion diseases. Herein, taking normal cellular form of prion (PrP^{C}) as a model owing to a high risk of pathogenicity of PrP^{Sc}, a new photoelectrochemical immunosensor has been developed based on hemin-induced switching of photocurrent direction. In the presence of PrP^{C}, nitrogen-doped porous carbon-hemin polyhedra labeled with secondary antibody were introduced onto the CdS-chitosan (CS) nanoparticles-modified indium–tin oxide (ITO) electrode via the antigen–antibody specific recognition. Because of the matched energy level between CdS and hemin, the high-efficiency switch of photocurrent direction of the ITO/CdS-CS photoelectrode from anodic to cathodic photocurrent was observed even at very low concentration (0.4 aM) of PrP^{C}. Through changing the specific antibody, this method can be easily expanded to PrP^{Sc} assay. Such low detectable limit is very useful in the early diagnosis and screening of prion diseases. The developed method has also promising applications in bioanalysis, disease diagnostics, and clinical biomedicine.

1. Introduction

Prion diseases, also called as Infectious spongiform encephalopathy, are fatal neurodegenerative and infectious disorders of humans and animals (Bruce et al., 1997; Ji and Zhang, 2010). Based on the protein-only hypothesis, conformational change from normal cellular form (PrP^{C}) into its pathogenic isoform (PrP^{Sc}) is a vital procedure in prion propagation (Lou et al., 2017a; Singh and Udgaonkar, 2015; Yu et al., 2016). Therefore, for the investigation of pathogenesis and early diagnosis of the prion disease, it is highly significant to ultrasensitively detect PrP^{Sc} at very low content. Up to now, many efforts have been devoted to prion assay, such as Western blot and enzyme-linked immunoassay (Ingrosso et al., 2002 (PrP^{Sc})), fluorescent assay (Xiao et al., 2010 (PrP^{Res} and PrP^{C})), surface plasmon resonance-based technology (Miodek et al., 2013a (PrP^{C}); Wan et al., 2009 (PrP^{Sc} and PrP^{C})), and electrochemical assay (Yu et al., 2015 (PrP^{C}); Miodek et al., 2013b (PrP^{C})). However, the lowest detection limit of these methods is at fM level, and some of them possess the drawbacks of complicated equipments, evident sample volume, and long operation. Recently, photoelectrochemical (PEC) method, as a newly burgeoning technique for sensitive assay, has received great attention, due to its simple instrumentation, good portability, and easy miniaturization (Zhang et al., 2018; Li et al., 2018a, 2018b; Yang et al., 2018a). Moreover, it exhibits superior performance in comparison with conventional methods, due to the advantage of complete separation of the light excitation source and photocurrent detection signal (Li et al., 2014; Wang et al., 2018a; Hu et al., 2018). However, only a few works, done in our group, focused on PrP^{C} assay by PEC method and the lowest detection limit was 29 fM (Yan et al., 2018; Li et al., 2018c). An ultrasensitive PEC means for prion protein assay is still highly desirable for early diagnostics of prion diseases.

In recent years, hemin (iron(III) protoporphyrin IX), the active center of heme-proteins (e.g., cytochrome, myoglobin and hemoglobin), has attracted extensive attention in biomimetic catalysis of simulated enzymes due to reversible transformation of Fe(III)/Fe(II) (Yuan et al., 2015; Zang et al., 2014). For example, Zang et al. reported a PEC sensing strategy for DNA detection by in-situ production of electron acceptors based on the catalytic reaction of hemin toward H_2O_2 (Zang et al., 2014). Moreover, hemin could also be as a receptor to capture the photogenerated electrons of p-type semiconductors to enhance cathodic photocurrents through the reduction of hemin[Fe(III)] to hemin[Fe(II)] (Wang et al., 2015; Lv et al., 2017). Wang et al. developed a PEC biosensing system based on hemin-intercalated G-quadruplex to enhance the cathodic photocurrents of PbS quantum dots (p-type) (Wang et al., 2015). Though hemin has fascinating properties to enhance cathodic photocurrents of p-type semiconductors, the direct

* Corresponding author.
E-mail address: chenjinhua@hnu.edu.cn (J. Chen).
[1] Ruiying Yang and Kang Zou contributed equally to this work.

https://doi.org/10.1016/j.bios.2019.02.035
Received 27 November 2018; Received in revised form 11 February 2019; Accepted 17 February 2019
Available online 21 February 2019
0956-5663/

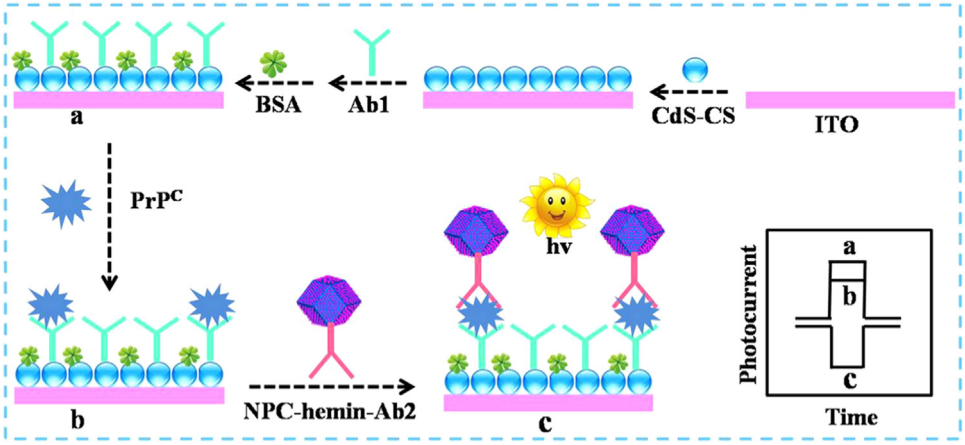

Scheme 1. Schematic illumination for PrP^C assay based on hemin-induced switching of photocurrent direction of PEC immunosensor.

interaction between hemin and n-type semiconductors is still not exploited for PEC analytical applications.

Herein, taking CdS-chitosan nanoparticles (CdS-CS NPs) as anodic photoactive materials due to a narrow band gap of n-type CdS (~2.4 eV) and many merits of chitosan (such as good adhesion and biocompatibility) (Wu et al., 2015; Yang et al., 2018b; He et al., 2017; Wang et al., 2018b), the effect of hemin on the PEC performance of CdS-CS NPs has been investigated. Interestingly, it was first time to find hemin-induced switching of photocurrent direction (from anodic to cathodic photocurrents) of CdS-CS NPs. Based on this phenomenon and nitrogen doped porous carbon (NPC) polyhedra as hemin support to further enhance the switch efficiency, a new PEC immunosensing platform was developed for the ultrasensitive detection of prion protein (Scheme 1). Because PrP^{Sc} has a high risk of pathogenicity, PrP^C was used as the model to evaluate the feasibility of the developed PEC immunosensor in PrP^{Sc} detection. As depicted in Scheme 1, CdS-CS NPs were modified on the indium–tin oxide (ITO) slice and showed a large anodic photocurrent. Then, PrP^C antibody (Ab1) was immobilized on the electrode with the assistance of glutaraldehyde. In the presence of PrP^C, NPC-hemin polyhedra labeled with secondary antibody of PrP^C (Ab2) were introduced onto the electrode based on the antigen–antibody specific recognition. Because of the matched energy level between CdS and hemin, the switch of photocurrent direction of the ITO/CdS-CS electrode from anodic to cathodic photocurrents was observed even at very low concentration (0.4 aM) of PrP^C. Through changing the specific antibody, the platform can be expediently expanded to PrP^{Sc} assay. To the best of our knowledge, no previous works reported such low detectable limit in either PrP^C or PrP^{Sc} assay. Such low detectable limit is very useful in the screening and early diagnosis of prion diseases. Additionally, the proposed PEC immunosensing platform had a linear response range from 4 aM to 40 fM. The developed method has also promising applications in disease diagnostics, bioanalysis, and clinical biomedicine.

2. Experimental section

2.1. Materials and reagents

ITO slices were supplied by Zhuhai Kaivo Electronic Components Co., Ltd (China). PrP^C (Human PrP^C (23-231), molecular weight 25.16 kDa), the native human cellular prion protein, was supplied by Jena Bioscience (Germany). The capture antibody (Ab1) of PrP^C, carbodiimide hydrochloride (EDC), N-hydroxysuccinimide (NHS) and bovine serum albumin (BSA) were supplied by Sigma Aldrich (USA). The secondary antibody (Ab2) of PrP^C was offered by Santa Cruz Biotechnology, Inc. (USA). Cadmium nitrate ($Cd(NO_3)_2{\cdot}4H_2O$), sodium sulfide ($Na_2S{\cdot}9H_2O$), zinc nitrate hexahydrate ($Zn(NO_3)_2{\cdot}6H_2O$), 2-methylimidazole, methanol (CH_3OH), chitosan (CS), ascorbic acid (AA) and glutaraldehyde were all offered by Sinopharm Chemical Reagent Co., Ltd. (China). Other chemicals were of analytical grade and used as received. The normal human serum was supplied by Anyan Inc. (Shanghai, China). All aqueous solutions were prepared with ultrapure water (> 18 MΩ cm) from a Milli-Q filtration system (Millipore Corp., USA).

2.2. Apparatus

The morphology and structure of the materials were investigated by scanning electron microscopy (SEM, JSM-6700F, Japan) equipped with an energy dispersive X-ray spectrometer (EDS) and transmission electron microscopy (TEM, JEM-2100F, Japan). X-ray diffraction (XRD) results were obtained on a Powder X-ray diffractometer (D/MAX-RA, Japan). Fourier transform infrared (FT-IR) spectra were tested by a Fourier transform spectrometer (NICOLET6700 FT-IR). The chemical composition of CdS-CS NPs and the chemical states of the related elements were analyzed by X-ray photoelectron spectroscopy (XPS, ESCALAB250Xi). Nitrogen adsorption–desorption isotherms and Brunauer–Emmett–Teller (BET) surface area of the material were tested using an ASAP 2020 Micrometrics sorptometer (USA). The UV–vis spectra were determined by a UV–vis spectrophotometer (UV-2500, LabTech). The light source was a Xe lamp (PLS-SXE300) fitted with a 420 nm filter. CHI 660D electrochemical workstation with a modified ITO electrode (diameter, 5.6 mm) as the working electrode, a saturated calomel electrode (SCE) as the reference electrode, and a platinum wire as the assistant electrode, was used in photoelectrochemical (PEC) and electrochemical impedance spectroscopic (EIS) investigations.

2.3. Preparation of CdS-CS NPs

10 mL of $Cd(NO_3)_2$ (0.1 M) methanol solution was poured into 10 mL of CS (0.5% m/v) solution under stirring for 30 min. Then, 11 mL of Na_2S (0.1 M) methanol/water mixture (1:1,v/v) was poured into the above solution under vigorously stirring for another 3 h. After that, the synthetic products were centrifuged, washed with methanol and water. Finally, the obtained CdS-CS NPs were dispersed in 400 mL water.

2.4. Preparation of NPC-hemin-Ab2 conjugates

ZIF-8-derived NPC polyhedra were prepared according to the previous work with minor modifications (Gai et al., 2013). In brief, 2-methylimidazole (3.280 g) and $Zn(NO_3)_2{\cdot}6(H_2O)$ (1.485 g) were respectively dissolved in CH_3OH (250 mL). After the 2-methylimidazole solution was fast added into the $Zn(NO_3)_2$ solution under agitation, the mixture was stirred for 2 h at room temperature. Finally, the

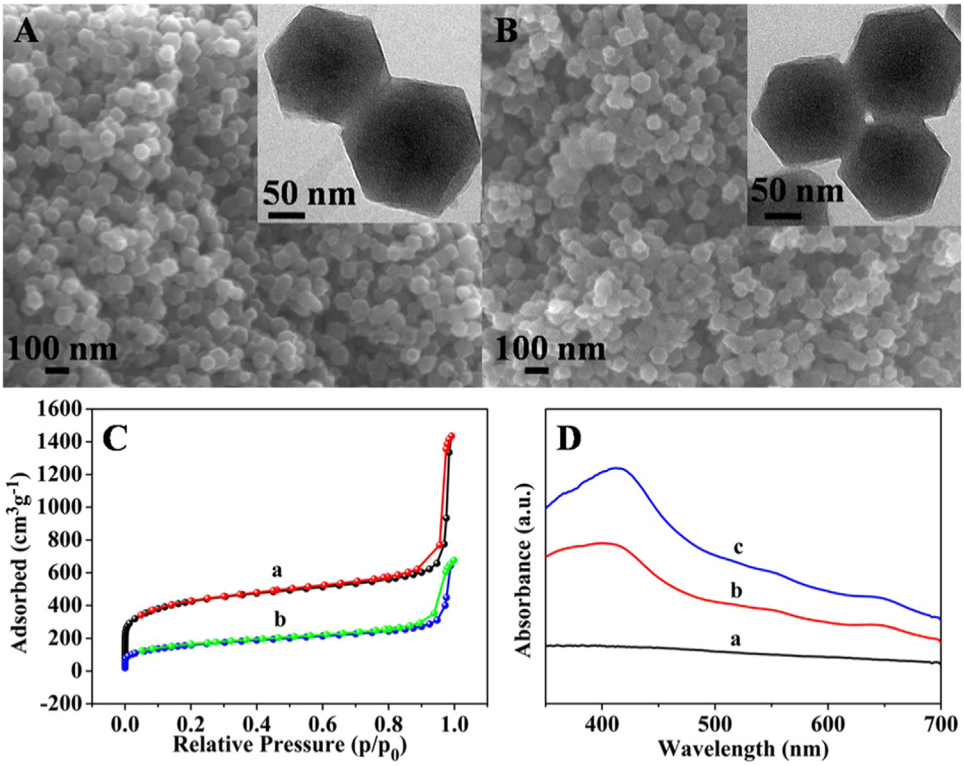

Fig. 1. SEM images of (A) NPC polyhedra and (B) NPC-hemin polyhedra, (C) The nitrogen adsorption-desorption isotherms of (a) NPC polyhedra and (b) NPC-hemin polyhedra. (D) UV–vis spectra of (a) NPC polyhedra, (b) hemin and (c) NPC-hemin polyhedra. Inset plots of A and B are the TEM images of NPC and NPC-hemin polyhedra, respectively.

precipitates (ZIF-8 polyhedra) were obtained via centrifugation, washed with CH_3OH, and then freeze-dried overnight. NPC polyhedra were synthesized by carbonization of ZIF-8 polyhedra under a flow of nitrogen gas at 1000 °C for 2 h with a heating rate of 5 °C min^{-1}.

2.4.1. For the preparation of NPC-hemin polyhedra

2.0 mL hemin (10 mM) in DMF was introduced into 5.0 mL aqueous solution containing NPC polyhedra (1 mg mL^{-1}) and the mixture solution was incubated for 24 h with slight stirring at room temperature. After being centrifuged and washed with PBS several times, the obtained NPC-hemin polyhedra were re-dispersed in 5.0 mL PBS (10 mM, pH 7.4).

2.4.2. For the preparation of NPC-hemin-Ab2 conjugates

2 mL of the above NPC-hemin polyhedra suspension was mixed with 500 μL of EDC (400 mM) and NHS (100 mM) in PBS (10 mM, pH 7.4) and the mixture solution was incubated for 20 min at room temperature. After centrifugation and re-dispersion in 2 mL PBS (10 mM, pH 7.4), 500 μL Ab2 (200 μg mL^{-1}) was added, and then the mixture was incubated for 12 h at room temperature. After being centrifuged and washed with PBS several times, the NPC-hemin-Ab2 conjugates were re-dispersed in 2 mL PBS (pH 7.4, 10 mM) with 2 wt% BSA, and then stored in 4 °C until use. Also, hemin-Ab2 conjugates were prepared according to a similar process.

2.5. Fabrication of the PEC immunosensor

Before use, the ITO electrode was pre-treated according to the previous work (Yang et al., 2017). To obtain the ITO/CdS-CS electrode, the above CdS-CS NPs suspension (25 μL) was coated onto the surface of the cleaned ITO electrode and dried in air. Subsequently, glutaraldehyde solution (20 μL, 2.5 wt%) was dropped onto the surface of the ITO/CdS-CS electrode for 0.5 h. For the immobilization of Ab1, 20 μL of Ab1 solution (20 μg mL^{-1}) was dropped onto the glutaraldehyde-treated ITO/CdS-CS electrode surface for 2 h. After that, the ITO/CdS-CS/Ab1 electrode was immersed into BSA (1 wt%) for 1 h to block the possible remaining active sites.

2.6. PEC assay

The obtained ITO/CdS-CS/Ab1/BSA electrodes were incubated with 20 μL of PBS (10 mM, pH 7.4) containing various concentrations of PrP^C for 60 min at 37 °C to obtain ITO/CdS-CS/Ab1/BSA/PrP^C electrode. Finally, the obtained electrodes were incubated with the above NPC-hemin-Ab2 suspension (20 μL) at 37 °C for 60 min. After cleaning with ultrapure water to take away the unbound NPC-hemin-Ab2 conjugates, the ITO/CdS-CS/Ab1/BSA/PrP^C/NPC-hemin-Ab2 electrodes were obtained. Finally, the PEC assay was performed in 0.1 M Tris–HCl solution (pH 7.4) containing 0.1 M AA at 0 V.

3. Results and discussion

3.1. Characterization of CdS-CS NPs

The morphology and microstructure of CdS-CS NPs were characterized by transmission electron microscopy (TEM). As shown in Fig. S1A (see Supplementary material section), the CdS-CS NPs have irregular shapes and its diameter is about 8 nm. A high-resolution TEM (HRTEM) image (Fig. S1B, see Supplementary material section) shows lattice spaces of 0.336 and 0.204 nm, which match well with the lattice spaces of (111) and (220) planes in CdS (JCPDS 10-0454), respectively. The successful preparation of CdS-CS NPs is further confirmed by the results of XRD, FT-IR, XPS and EDS (Figs. S1C-S1D, Fig. S2 and Fig. S3A, see Supplementary material section). Additionally, from the UV–vis absorption spectrum of CdS-CS NPs (the insert plot of Fig. S1A, see Supplementary material section), a broad absorption range below 568 nm can be observed, indicating its good absorption properties to visible light (Wang et al., 2018c; Shen et al., 2010). On the other hand, the ITO/CdS-CS electrode were further investigated by EIS method, and the corresponding results are shown in Fig. S3B (see Supplementary material section). It is noted that the electron transfer properties of the ITO/CdS-CS electrode is slightly inferior to that of the ITO electrode

due to the non-excellent electronic conductivity of CdS-CS NPs. However, it is still satisfactory for the ITO/CdS-CS electrode to be a photoelectrode in PEC assay.

3.2. Characterization of NPC-hemin polyhedra

Fig. 1 shows the SEM and TEM images of the NPC and NPC-hemin polyhedra. As can be seen from Fig. 1A, the NPC polyhedra show the typical rhombic dodecahedron morphology with the average size of ~120 nm. Moreover, Fig. 1B shows that the synthesized NPC-hemin polyhedra have the same morphology and average size as the parent NPC (Fig. 1A). These imply that hemin may be encapsulated in the pores of the NPC polyhedra. In order to clarify this guess, the porosity of the NPC and NPC-hemin polyhedra were measured by the nitrogen adsorption-desorption isotherms. From Fig. 1C, the Brunauer–Emmett–Teller (BET) surface areas of NPC and NPC-hemin polyhedra are calculated to be 1498.6 and 578.1 $m^2\ g^{-1}$, respectively. The corresponding total pore volumes are 1.201 and 0.619 $cm^3\ g^{-1}$, respectively. This indicates clearly that hemin is filled in the pores of NPC polyhedral (Luo et al., 2015). Furthermore, the UV–vis absorption spectroscopy was used to investigate the NPC polyhedra, hemin and NPC-hemin polyhedra (Fig. 1D). Hemin features a strong absorption peak at ~ 400 nm together with weak peaks at 551 and 646 nm (curve b) (Xue et al., 2012). After hemin is filled in the pores of NPC polyhedra, the strong absorption peak of the NPC-hemin polyhedra is at 412 nm, and the weak peaks occur at the same wavelengths (curve c). The encapsulation of hemin in NPC polyhedra leads to a small red shift of the maximum absorption band for about 12 nm, due to the molecular flattening (Xu et al., 2009). However, NPC polyhedra have no obvious absorption peaks (curve a). The results from Fig. 1D further indicate that hemin is successfully filled in the NPC polyhedra.

3.3. Hemin-induced switching of photocurrent direction of the ITO/CdS-CS photoelectrode

The PEC properties of the ITO/CdS-CS, ITO/hemin, ITO/CdS-CS/hemin and ITO/CdS-CS/NPC electrodes have been investigated. From Fig. 2A, the photocurrents of the ITO/CdS-CS electrode (curve a) and ITO/hemin (curve b) are 3.769 μA and -2.932×10^{-3} μA, respectively. However, the photocurrent of the ITO/CdS-CS/hemin electrode is −3.013 μA (curve c), which is opposite to the photocurrent direction of the ITO/CdS-CS electrode. Additionally, the photocurrent of ITO/CdS-CS/NPC electrode (4.126 μA, curve d) is slightly larger than that of the ITO/CdS-CS electrode, due to the good electronic conductivity of the NPC polyhedra. Noteworthily, the cathodic photocurrent of the ITO/CdS-CS/hemin electrode (curve c) is 1000 times larger than that of the ITO/hemin electrode (curve b), indicating that hemin has excellent ability to switch photocurrent direction of the ITO/CdS-CS electrode from anodic to cathodic currents.

The possible reasons may be as follows: Under visible light illumination, CdS is excited and the correspondingly photogenerated holes/electrons are formed on the valence band (VB)/conduction band (CB). The photogenerated electrons transfer from the CB of CdS to the ITO electrode, and photogenerated holes oxidize AA to decrease the electron-hole recombination and to promote the generation of photogenerated electrons, resulting in a large anodic photocurrent (Fig. 2B). When hemin is present in the ITO/CdS-CS system, the photocurrent direction of the ITO/CdS-CS electrode is changed from anodic to cathodic photocurrents due to the matched energy level between CdS and hemin (Fig. 2C).

In order to clarify clearly this phenomenon, the VB and CB edges of CdS were investigated by electrochemical method (Wang et al., 2015; Yeh et al., 2013). The VB and CB edges of CdS can be observed at 1.06 V and − 1.02 V vs. SCE (Figs. S4A and S4B, see Supplementary material section). However, the hemin reveals a reduction peak at − 0.40 V vs. SCE (Fig. S4C, see Supplementary material section) according to the Fe^{II}/Fe^{III} −protoporphyrin IX couple, which is roughly consistent with that reported in the previous literature (Zhang et al., 2013). It is noted that the reduction peak potential of hemin is more positive than the CB level of CdS, indicating that a potential gradient exists to drive the photoelectron transmission from the CB of CdS (−1.02 V vs. SCE) to hemin (−0.40 V vs. SCE). This results in the switch of photocurrent direction of the ITO/CdS-CS photoelectrode from anodic to cathodic photocurrents. Moreover, cyclic voltammograms of the hemin-modified electrode in air-saturated solution indicate that the oxidation peak current of hemin decreases largely and a conspicuously increased reduction peak is obtained (Fig. S4C, curve b, see Supplementary material section), and the reduction peak current of hemin in air-saturated solution is much larger than that in N_2-saturated solution (Fig. S4C, curve a, see Supplementary material section). This phenomenon may demonstrate that hemin acts as a mediator for the catalytic reduction of O_2 besides an electron acceptor. After accepting photogenerated electrons from the excited CdS, hemin(III) is reduced to hemin(II). The hemin(II) lightly reacts with O_2 to revive hemin(III) by the reduction of O_2 (Wang et al., 2015; Deng et al., 2013). Based on these processes, the electron-hole recombination on the illuminated CdS is restrained and an enhanced cathodic photocurrent is obtained (curve c in Fig. 2A). In order to introduce hemin to the electrode surface for prion assay and to further enhance the switch effect of hemin, NPC-hemin-Ab2 conjugates were used in the following experiments.

3.4. EIS and PEC investigation of the preparation of PEC immunosensor

Electrochemical impedance spectroscopy (EIS) is a useful technique to investigate the modified processes of the electrode (Yan et al., 2015). In EIS results, the semicircle diameter of the Nyquist diagram shows the

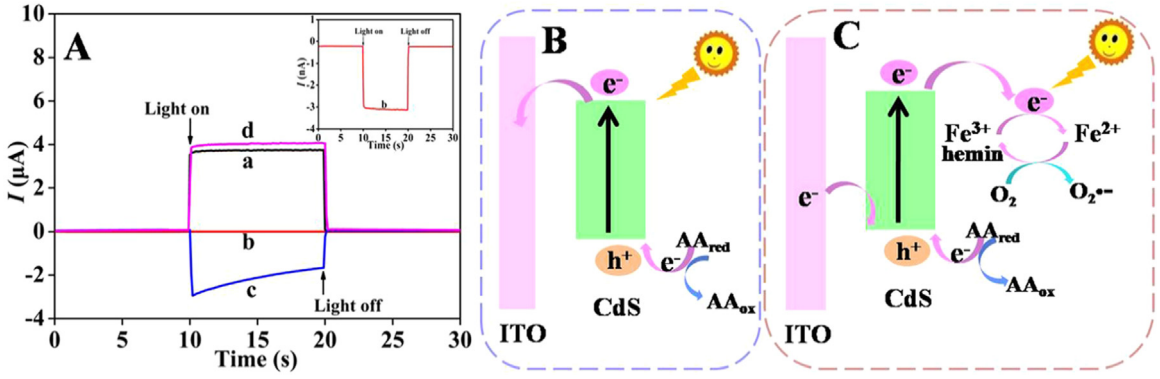

Fig. 2. (A) Photocurrents of (a) ITO/CdS-CS, (b) ITO/hemin, (c) ITO/CdS-CS/hemin and (d) ITO/CdS-CS/NPC electrodes. Hemin, 0.03 mg; NPC, 0.02 mg. (B) The photocurrent generation mechanism of ITO/CdS-CS electrode. (C) The photocurrent generation mechanism of ITO/CdS-CS/hemin electrode. Insets of A is the photocurrent of (b) ITO/hemin electrode.

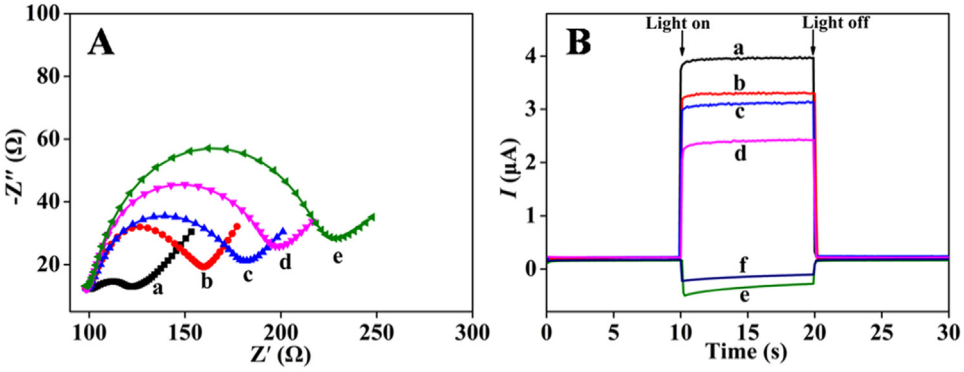

Fig. 3. (A) EIS results of the different electrodes in 0.1 M KCl + 5 mM (1:1) $[Fe(CN)_6]^{3-/4-}$ solution. Frequency range, 0.1–100 kHz; Amplitude, 5 mV. (B) Photocurrent responses of the different electrodes at 0 V in Tris–HCl (0.1 M, pH 7.4) + 0.1 M AA solution. (a) ITO/CdS-CS, (b) ITO/CdS-CS/Ab1, (c) ITO/CdS-CS/Ab1/BSA, (d) ITO/CdS-CS/Ab1/BSA/PrP^C, (e) ITO/CdS-CS/Ab1/BSA/PrP^C/NPC-hemin-Ab2, (f) ITO/CdS-CS/Ab1/BSA/PrP^C/hemin-Ab2. (PrP^C, 4000 aM).

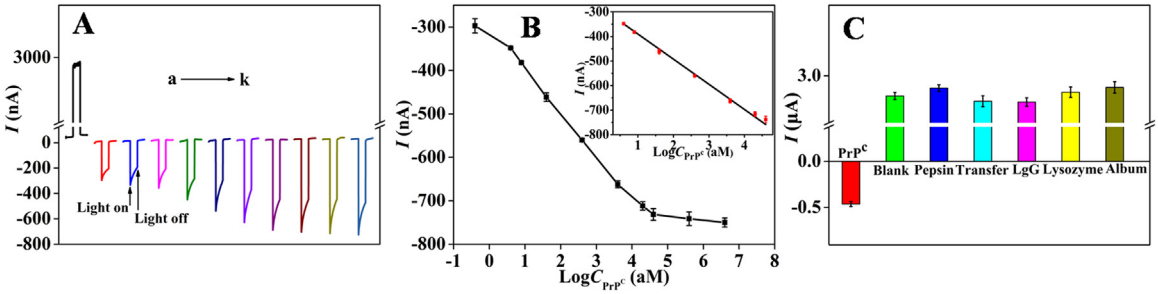

Fig. 4. (A) Photocurrent responses of the PEC sensing platform toward the various concentrations of PrP^C. The concentrations are (from a to k) 0, 0.4, 4, 8, 4×10^1, 4×10^2, 4×10^3, 2×10^4, 4×10^4, 4×10^5 and 4×10^6 aM. (B) Dependence of *I* on the PrP^C concentrations. (C) Selectivity of the developed PEC immunosensor. PrP^C, 40 aM; other proteins (pepsin, transferrin, IgG, lysozyme and HSA), 4000 aM.

Table 1
Comparison of different methods for prion detection.

Method	Linear range	Limit of Detection	Sensitivity[a]	Reference
Fluorescence	44–1800 nM	12 nM	147.5 μM^{-1}	Xiao et al. (2009)
	800–306000 pM	85.5 pM	0.30 nM^{-1}	Xiao et al. (2010)
Surface plasmon resonance	4–4×10^9 fM	4 fM	7.639 RU fM^{-1}	Lou et al. (2017a)
	40–4×10^5 fM	40 fM	0.933 RU fM^{-1}	Lou et al. (2017b)
	400–4×10^5 fM	–	24.606 RU pM^{-1}	Lou et al. (2018)
	870–21700 pM	570 pM	22.59 RU nM^{-1}	Wan et al. (2009)
Electrochemi-stry	20–280 fM	7.6 fM	92.6 nA fM^{-1}	Yu et al. (2016)
	15–1500 fM	2.1 fM	100 nA fM^{-1}	Li et al. (2017a)
	200–2000 fM	160 fM	1.111 pM^{-1}	Yu et al. (2015)
	3–4000 fM	0.56 fM	1000 nA fM^{-1}	Li et al. (2017b)
	1–10^7 pM	0.5 pM	4.953 nM^{-1}	Miodek et al. (2013b)
	1–1000 pM	0.8 pM	16.7 nM^{-1}	Miodek et al. (2014)
Photoelectr-ochemistry	200–2000 fM	50.9 fM	0.170 nA fM^{-1}	Yan et al. (2018)
	39–1987 fM	29 fM	0.084 nA fM^{-1}	Li et al. (2018c)
	4–4×10^4 aM	0.4 aM (detectable limit)	8.450 nA aM^{-1} (8450 nA fM^{-1})	This work

[a] The maximum sensitivity.

interfacial charge-transfer resistance (R_{ct}) of the electrode. It is noted that the R_{ct} value of the ITO/CdS-CS electrode is 63.7 Ω (Fig. 3A, curve a). When the electrode is modified orderly with Ab1 and BSA, the R_{ct} values increase to 91.3 Ω (Fig. 3A, curve b) and 104.8 Ω (Fig. 3A, curve c), respectively, because of the nonconductive protein molecules. From curve d in Fig. 3A, an enhanced R_{ct} value (126.8 Ω) can be observed when the ITO/CdS-CS/Ab1/BSA electrode is further incubated with PrP^C. After incubation with NPC-hemin-Ab2 solution, the NPC-hemin-Ab2 conjugates are introduced to the immunosensing platform on the basis of the specific interaction between PrP^C and Ab2 on the NPC-hemin polyhedra, leading to an increasing R_{ct} value (148.7 Ω, Fig. 3A, curve e) because of the effect of steric hindrance from the NPC-hemin-Ab2 conjugates. The above EIS results suggest the successful construction of the proposed PrP^C immunosensor according to Scheme 1.

To further trace the fabricating process of the developed PEC immunosensor, PEC characterization was also carried out. As displayed in Fig. 3B, the ITO/CdS-CS electrode reveals a strong anodic photocurrent (curve a), because of the desirable photoelectric properties of CdS-CS NPs. Subsequent introduction of Ab1, BSA and PrP^C on the ITO/CdS-CS electrode, the photocurrents obviously decrease (curves b–d). These results are in conformity with that obtained in EIS experiments (Fig. 3A). However, when the immunosensor is incubated with NPC-hemin-Ab2 or hemin-Ab2, leading to obvious cathodic photocurrents (−667 nA, curve e; −425 nA, curve f), due to the impactful transmission of photogenerated electrons/holes through the matched energy levels between CdS and hemin. Obviously, the cathodic photocurrent for the NPC-hemin-Ab2 is larger than that for the hemin-Ab2, because NPC polyhedra with porous structure and high surface area can load more hemin for enhancing cathodic photocurrent. These results demonstrate that the PEC analytical system has been constructed successfully for PrP^C detection (Scheme 1).

3.5. PEC assay of PrP^C

To achieve the optimal assay performance of the proposed immunosensor for the ultrasensitive detection of PrP^C, The experimental parameters (the Ab1 concentration, the incubation time of PrP^C, and the mass ratio between Ab2 and NPC-hemin) were optimized (Figs. S5A-S5C, see Supplementary material section). Under optimal experimental conditions, a series of PrP^C solutions with different concentrations were measured. From Fig. 4A, an anodic photocurrent (2.932 μA) of the electrode is changed to cathodic photocurrent (−0.298 μA), when a trace PrP^C (0.4 aM) is present in the assay solution. The reasons for such low detectable limit may be as follows: the matching of the energy levels between CdS and hemin results in the high-efficiency switch of photocurrent direction of the ITO/CdS-CS electrode and NPC polyhedra with porous structure and high surface area can load large amounts of hemin. These lead to the change of the photocurrent from anodic to cathodic currents even at such low concentration of PrP^C. As we all know, via changing the specific antibody, this platform can be easily expanded to PrP^{Sc} assay. Such low detectable limit should be very useful in the screening and early diagnosis of prion diseases.

Fig. 4B shows the dependence of the photocurrent of the developed biosensor on the concentration of PrP^C. A linear relationship between the value of the cathodic photocurrent (I) and PrP^C concentration can be obtained from 4 to 4×10^4 aM with a linear equation of $I = -102.4 \log C_{PrP^C} - 287.5$ ($R^2 = 0.9975$). Compared with the previously reported methods, the developed PEC immunosensor shows wider linear response range at the low concentration range and much higher sensitivity, and the detectable limit obtained in this work is 1400 times lower than the calculated detection limit reported previously (Table 1). This may be beneficial to PrP^{Sc} assay when the specific antibody of PrP^C is changed to that of PrP^{Sc} because of the very low concentration of PrP^{Sc} existed in prion-infected samples.

To demonstrate the selectivity of the proposed immunosensor for PrP^C detection, several possible interfering proteins, including pepsin, transferrin, IgG, lysozyme and human serum albumin (HSA) were selected. Compared with the blank solution, the interfering proteins do not change the photocurrent direction of the PEC immunosensor and no significant changes of the anodic photocurrent responses are observed (Fig. 4C). However, when the target PrP^C (40 aM) is present, the anodic photocurrent of the developed PEC immunosensor is changed to a cathodic photocurrent due to the fact that PrP^C could specifically carry out antigen-antibody interaction between PrP^C and its antibodies, implying a high selectivity of the prepared PEC immunosensor. The results shown in Fig. 4C also indicate that the developed PEC immunosensor has excellent characteristics on the elimination of the false positive signal. On the other hand, the developed PEC immunosensor shows satisfactory reproducibility and acceptable stability (see Supplementary material section), and satisfactory recovery in complex biological system (see Supplementary material section, Table S1).

4. Conclusions

Based on the hemin-induced switching of photocurrent direction of the ITO/CdS-CS electrode, a new PEC immunosensor has been developed for sensitive and selective assay of prion. In the presence of PrP^C, NPC-hemin-Ab2 conjugates are introduced to the surface of the ITO/CdS-CS photoelectrode by the antigen–antibody specific recognition. The matching of the energy levels between CdS and hemin results in the high-efficiency switch of photocurrent direction of the ITO/CdS-CS electrode from anodic to cathodic photocurrents. The developed PEC immunosensor shows a detectable limit as low as 0.4 aM. Till now, no previous works reported such low detectable limit in either PrP^C or PrP^{Sc} assay. By changing the specific antibody of PrP^C to that of PrP^{Sc}, this platform can be easily expanded to PrP^{Sc} assay and such low detectable limit is very useful in the screening and early diagnosis of prion diseases. On the other hand, the developed PEC immunosensor has a wide linear response range from 4 aM to 40 fM, and shows satisfactory reproducibility, acceptable stability and good selectivity. We believe that the hemin-induced photocurrent direction switching system presented in this study would have promising applications in bioanalysis, disease diagnostics, and clinical biomedicine.

CRediT authorship contribution statement

Ruiying Yang: Investigation, Methodology, Data curation, Writing - original draft. **Kang Zou:** Investigation, Methodology, Data curation. **Xiaohua Zhang:** Validation, Data curation. **Cuicui Du:** Writing - review & editing. **Jinhua Chen:** Conceptualization, Supervision, Writing - review & editing.

Acknowledgements

This work was financially supported by NSFC (21475035, 21727810), and the Foundation for Innovative Research Groups of NSFC (21521063).

Declaration of interests

None.

Appendix A. Supporting information

Supplementary data associated with this article can be found in the online version at doi:10.1016/j.bios.2019.02.035.

References

Bruce, M.E., Will, R.G., Ironside, J.W., McConnell, I., Drummond, D., Suttie, A., McCardle, L., Chree, A., Hope, J., Birkett, C., Cousens, S., Fraser, H., Bostock, C.J., 1997. Nature 389, 498–501.
Deng, S.Y., Cheng, L.X., Lei, J.P., Cheng, Y., Huang, Y., Ju, H.X., 2013. Nanoscale 5, 5435–5441.
Gai, P.B., Zhang, H.J., Zhang, Y.S., Liu, W., Zhu, G.B., Zhang, X.H., Chen, J.H., 2013. J. Mater. Chem. B 1, 2742–2749.
He, X.M., Liang, X.C., Chen, X., Yuan, B.F., Zhou, P., Zhang, L.N., Feng, Y.Q., 2017. Anal. Chem. 89, 9712–9721.
Hu, T., Zheng, Y.N., Li, M.J., Liang, W.B., Chai, Y.Q., Yuan, R., 2018. Anal. Chem. 90, 6096–6101.
Ingrosso, L., Vetrugno, V., Cardone, F., Pocchiari, M., 2002. Trends Mol. Med. 8, 273–280.
Ji, H., Zhang, H., 2010. Trends Biochem. Sci. 35, 129–134.
Li, R.Z., Liu, Y., Cheng, L., Yang, C.Z., Zhang, J.D., 2014. Anal. Chem. 86, 9372–9375.
Li, X.Y., Li, J.J., Liu, Y.Q., Zhang, X.H., Chen, J.H., 2017a. Sens. Actuators B 241, 151–159.
Li, J.J., Yan, X.X., Li, X.Y., Zhang, X.H., Chen, J.H., 2017b. Talanta 179, 726–733.
Li, R.Y., Tu, W.W., Wang, H.S., Dai, Z.H., 2018a. Anal. Chem. 90, 9403–9409.
Li, M.J., Xiong, C., Zheng, Y.N., Liang, W.B., Yuan, R., Chai, Y.Q., 2018b. Anal. Chem. 90, 8211–8216.
Li, Y.M., Meng, L.X., Zou, K., Zhang, X.H., Chen, J.H., 2018c. J. Electroanal. Chem. 829, 51–58.
Lou, Z.C., Han, H., Zhou, M., Wan, J.F., Sun, Q., Zhou, X.Y., Gu, N., 2017a. Anal. Chem. 89, 13472–13479.
Lou, Z.C., Sun, J.Q., Wan, J.F., Zhang, X.H., Zhang, H.Q., Gu, N., 2017b. J. Nano Res. 48, 18–28.
Lou, Z.C., Han, H., Mao, D., Jiang, Y.B., Song, J.Y., 2018. Nanomaterials 8, 107.
Luo, F.Q., Lin, Y.L., Zheng, L.Y., Lin, X.M., Chi, Y.W., 2015. ACS Appl. Mater. Interfaces 7, 11322–11329.
Lv, S.Z., Zhang, K.Y., Lin, Z.Z., Tang, D.P., 2017. Biosens. Bioelectron. 96, 317–323.
Miodek, A., Poturnayová, A., Snejdárková, M., Hianik, T., Korri-Youssoufi, H., 2013a. Anal. Bioanal. Chem. 405, 2505–2514.
Miodek, A., Castillo, G., Hianik, T., Korri-Youssoufi, H., 2013b. Anal. Chem. 85, 7704–7712.
Miodek, A., Castillo, G., Hianik, T., Korri-Youssouf, H., 2014. Biosens. Bioelectron. 56, 104–111.
Shen, R., Shen, X.Q., Zhang, Z.M., Li, Y.S., Liu, S.Y., Liu, H.W., 2010. J. Am. Chem. Soc. 132, 8627–8634.
Singh, J., Udgaonkar, J.B., 2015. Angew. Chem. Int. Ed. 54, 1–6.
Wan, J., Wang, X., Li, J., Liu, W., Xu, M., Liu, L., Xu, J., Wang, H., Gao, H., 2009. Arch. Virol. 154, 1901–1908.
Wang, G.L., Shu, J.X., Dong, Y.M., Wu, X.M., Zhao, W.W., Xu, J.J., Chen, H.Y., 2015. Anal. Chem. 87, 2892–2900.
Wang, Z.Y., Liu, J., Liu, X., Shi, X.Y., Dai, Z.H., 2018a. Anal. Chem. https://doi.org/10.1021/acs.analchem.8b03195.

Wang, G.L., Yuan, F., Gu, T.T., Dong, Y.M., Wang, Q., Zhao, W.W., 2018b. Anal. Chem. 90, 1492–1497.
Wang, Q., Ruan, Y.F., Zhao, W.W., Lin, P., Xu, J.J., Chen, H.Y., 2018c. Anal. Chem. 90, 3759–3765.
Wu, K.F., Du, Y.L., Tang, H., Chen, Z.Y., Lian, T.Q., 2015. J. Am. Chem. Soc. 137, 10224–10230.
Xiao, S.J., Hu, P.P., Li, Y.F., Huang, C.Z., Huang, T., Xiao, G.F., 2009. Talanta 79, 1283–1286.
Xiao, S.J., Hu, P.P., Wu, X.D., Zou, Y.L., Chen, L.Q., Peng, L., Ling, J., Zhen, S.J., Zhan, L., Li, Y.F., Huang, C.Z., 2010. Anal. Chem. 82, 9736–9742.
Xu, Y.X., Zhao, L., Bai, H., Hong, W.J., Li, C., Shi, G.Q., 2009. J. Am. Chem. Soc. 131, 13490–13497.
Xue, T., Jiang, S., Qu, Y.Q., Su, Q., Cheng, R., Dubin, S., Chiu, C.Y., Kaner, R., Huang, Y., Duan, X.F., 2012. Angew. Chem., Int. Ed. 124, 3888–3891.
Yan, K., Liu, Y., Yang, Y.H., Zhang, J.D., 2015. Anal. Chem. 87, 12215–12220.
Yan, X.X., Li, J.J., Yang, R.Y., Li, Y.M., Zhang, X.H., Chen, J.H., 2018. Sens. Actuators B. 255, 2187–2193.
Yang, R.Y., Yan, X.X., Li, Y.M., Zhang, X.H., Chen, J.H., 2017. ACS Appl. Mater. Interfaces 9, 42482–42491.
Yang, R.Y., Zou, K., Li, Y.M., Meng, L.X., Zhang, X.H., Chen, J.H., 2018a. Anal. Chem. 90, 9480–9486.
Yang, R.Y., Li, Y.M., Zou, K., Yan, X.X., Meng, L.X., Zhang, X.H., Chen, J.H., 2018b. Chem. Commun. 54, 4830–4833.
Yeh, T.F., Chen, S.J., Yeh, C.S., Teng, H., 2013. J. Phys. Chem. C. 117, 6516–6524.
Yu, P., Zhang, X.H., Zhou, J.W., Xiong, E.H., Li, X.Y., Chen, J.H., 2015. Sci. Rep. 5, 16015–16023.
Yu, P., Zhang, X.H., Xiong, E.H., Zhou, J.W., Li, X.Y., Chen, J.H., 2016. Biosens. Bioelectron. 85, 471–478.
Yuan, L., Tu, W.W., Bao, J.C., Dai, Z.H., 2015. Anal. Chem. 87, 686–692.
Zang, Y., Lei, J.P., Zhang, L., Ju, H.X., 2014. Anal. Chem. 86, 12362–12368.
Zhang, L.B., Zhu, J.B., Guo, S.J., Li, T., Li, J., Wang, E.K., 2013. J. Am. Chem. Soc. 135, 2403–2406.
Zhang, L., Zhu, Y.C., Liang, Y.Y., Zhao, W.W., Xu, J.J., Chen, H.Y., 2018. Anal. Chem. 90, 5439–5444.